Electronic Supplementary Material (ESI) for Nanoscale.

Supplementary Information for

Kinetic Pathways Towards Mass Production of Single Crystalline Stanene on Topological Insulator Substrates

Liying Zhang,[a,b] Wei Qin,[b] Leiqiang Li,[b] Shunfang Li,*[a] Ping Cui,*[b,c] Yu Jia,[a] and Zhenyu Zhang[b]

[a]*School of Physics and Engineering, Zhengzhou University, Zhengzhou 450001, China*

[b]*International Center for Quantum Design of Functional Materials (ICQD), Hefei National Laboratory for Physical Sciences at the Microscale, and Synergetic Innovation Center of Quantum Information and Quantum Physics, University of Science and Technology of China, Hefei, Anhui 230026, China*

[c]*Key Laboratory of Strongly-Coupled Quantum Matter Physics, Chinese Academy of Sciences, School of Physical Sciences, University of Science and Technology of China, Hefei, Anhui 230026, China*

*Corresponding authors:
Ping Cui: cuipg@ustc.edu.cn;
Shunfang Li: sflizzu@zzu.edu.cn.

Contents:

1. Supplemental figures

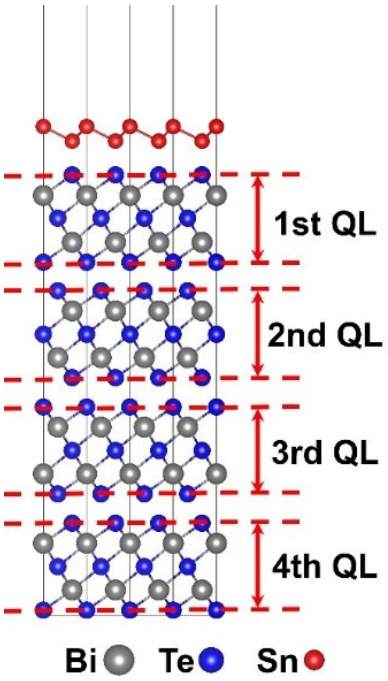

Fig. S1 Geometric structure of 1ML stanene on 4-QL Te-Bi_2Te_3(111). The four QLs of Te-Bi_2Te_3(111) are highlighted.

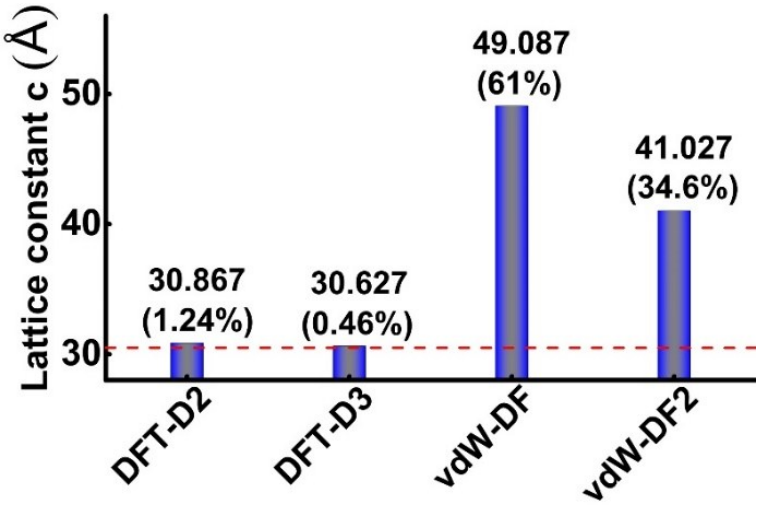

Fig. S2 Calculated lattice constant *c* of bulk Bi_2Te_3 within four different vdW correction schemes. The red dashed line shows the experimental value of 30.487 Å.[1] In the brackets, the inaccuracies of the calculations relative to the experimental value are also presented.

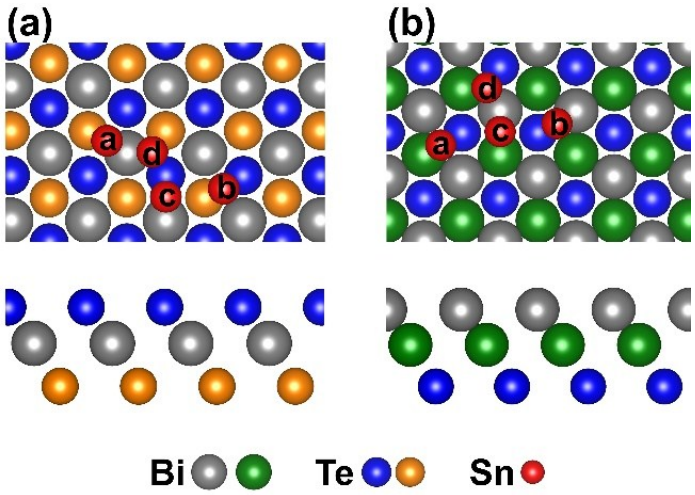

Fig. S3 Top (upper panels) and side (lower panels) views of four possible initial asymmetric adsorption sites of one Sn atom on (a) Te-Bi_2Te_3(111) and (b) Bi-Bi_2Te_3(111), labeled as **a**, **b**, **c**, and **d**, respectively.

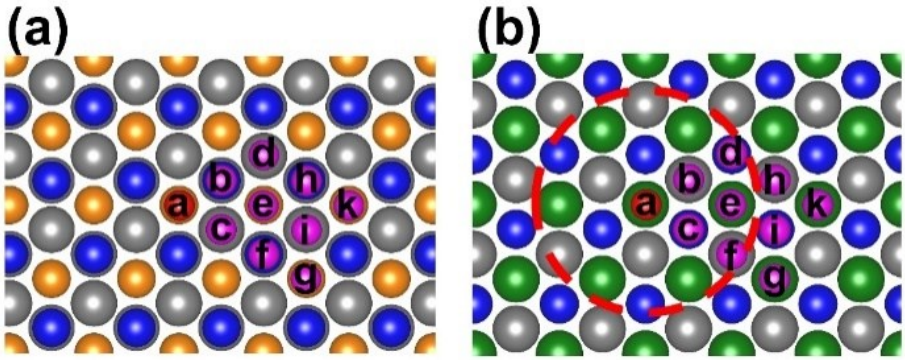

Fig. S4 Top views of possible initial high symmetry adsorption sites of two Sn atoms on (a) Te-Bi_2Te_3(111) and (b) Bi-Bi_2Te_3(111). The red sphere represents the first Sn adatom and is placed on the most stable adsorption site of fcc in (a) and hcp (b), in both cases labeled as **a**. The pink spheres represent the second Sn adatom and are chosen to be on nearby high symmetry sites within the Sn-Sn distance range of R(Sn-Sn) < 8.77 Å, in both cases labeled as **b**, **c**, **d**, **e**, **f**, **g**, **h**, **i**, and **k**. In (b), the red dashed circle with R(Sn-Sn) = 5.3 Å indicates that two Sn adatoms within this regime will always relax to nucleate into a dimer upon optimization. For the cases of the first Sn adatom at site **a** and the second Sn adatom at site **k** in both (a) and (b), larger (5×5) surface supercells were used in our DFT calculations.

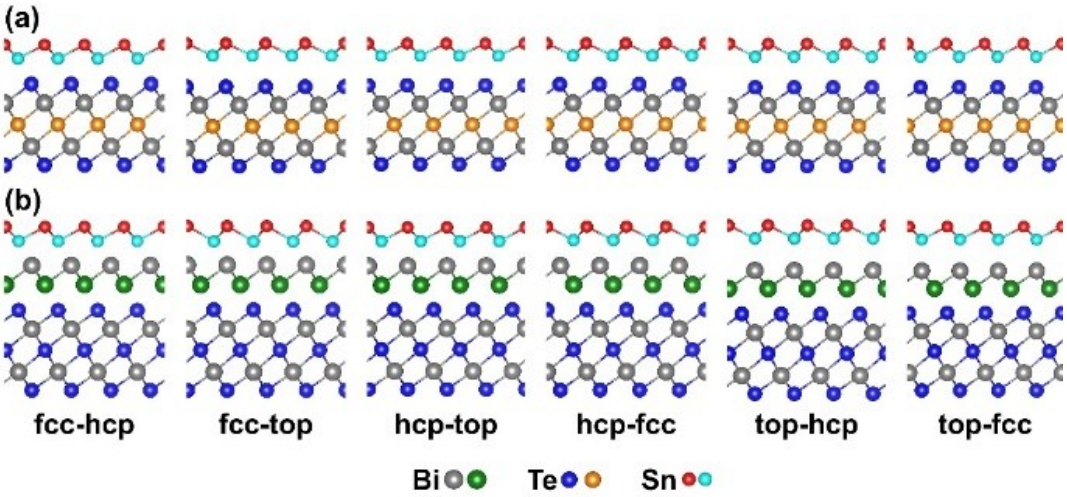

Fig. S5 Side views of six optimized high symmetry adsorption structures of 1ML stanene on (a) Te-Bi_2Te_3(111) and (b) Bi-Bi_2Te_3(111).

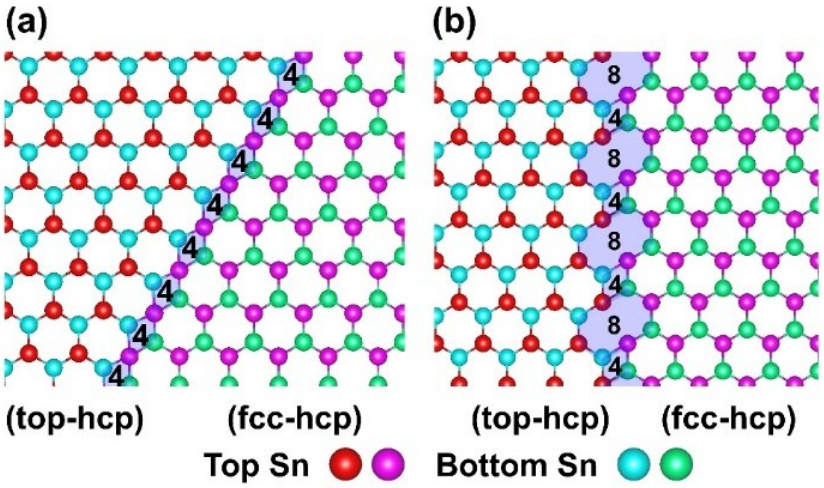

Fig. S6 Two possible GB patterns of a stanene overlayer grown on Te-Bi_2Te_3(111), formed along the (a) zigzag and (b) armchair edge directions of stanene. In (a), the GB contains 4-atom rings; in (b), the GB contains both 4-atom and 8-atom rings.

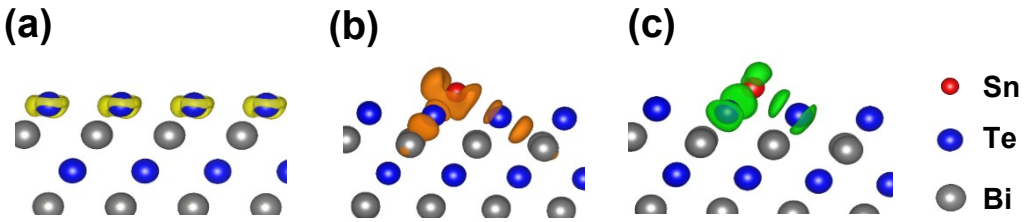

Fig. S7 (a) Charge density of the topological surface states (TSSs) of Te-Bi_2Te_3 at the Γ point. The isosurface value is 0.0004 e/Å^3. (b) Charge depletion (orange) and (c) charge accumulation (green) on the surface of Sn/Te-Bi_2Te_3 through differential charge density analysis. In (b) and (c), the isosurface value is 0.0015 e/Å^3.

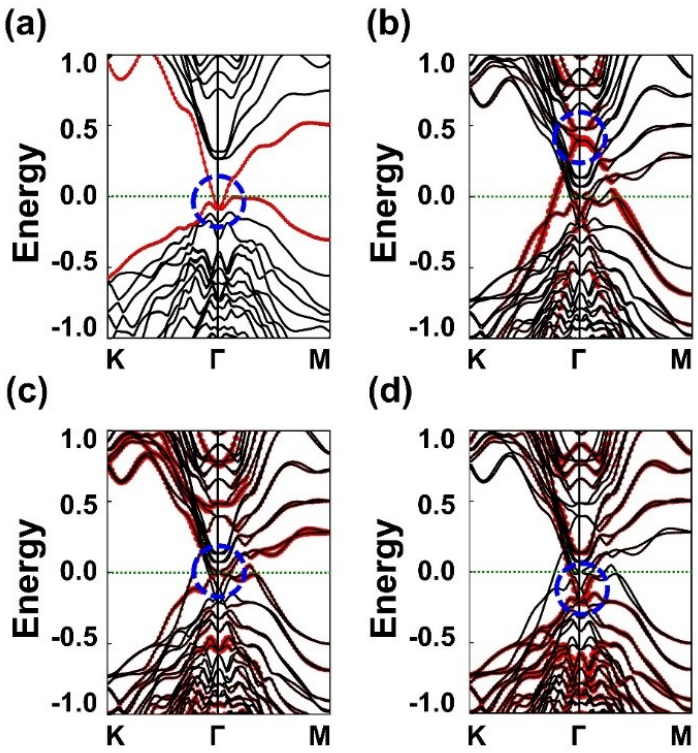

Fig. S8 Calculated band structures of (a) 4-QL Te-Bi_2Te_3(111) and (b)-(d) 4-QL Bi-Bi_2Te_3(111). The spectral weights contributed from the topmost surface Te atoms of Te-Bi_2Te_3(111) in (a) and the top Bi bilayer atoms in (b), the topmost QL in (c), and the bottommost QL in (d) of Bi-Bi_2Te_3(111) are highlighted by the red spheres. The blue dashed circles show the locations of the Dirac points of the topological surface states.

2. Pseudospin model analysis

Here we develop a pseudospin-based approach to identify the potential spin-orbit coupling (SOC)-induced band inversion around the K point in the present systems, namely, stanene grown on the Te-Bi_2Te_3 (111) or Bi-Bi_2Te_3 (111) substrates. The DFT calculations of their band structures are presented in Fig. 4 in the main text, where the bands around the K points are dominated by p_z orbitals of Sn atoms. In the absence of SOC, the band gap opening around the K point is mainly attributed to the presence of the substrate, inducing inequivalent chemical potentials on the top Sn (Sn_{top}) and bottom Sn (Sn_{bottom}) atoms of stanene and leading to the breaking of sublattice symmetry. In analogy with monolayer graphene[2,3], a low-energy "$k \cdot p$" effective model describing the physics around the K or K' point can be deduced as

$$h_0(\vec{k}) = v_F(\eta k_x \sigma_x + k_y \sigma_y) s_0, \quad (1)$$

$$h_{sub}(\vec{k}) = \delta\mu \sigma_z s_0, \quad (2)$$

$$h_{soc}(\vec{k}) = \eta \Delta \sigma_z s_z, \quad (3)$$

$$h_R(\vec{k}) = \frac{1}{2}\lambda(\eta \sigma_x s_y - \sigma_y s_x), \quad (4)$$

where v_F is the Fermi velocity, $\eta = \pm 1$ correspond to the K and K' points, respectively, s_0 is the 2×2 identity matrix, and $\vec{\sigma} = (\sigma_x, \sigma_y, \sigma_z)$ and $\vec{s} = (s_x, s_y, s_z)$ are Pauli matrices acting on the pseudospin and real spin, respectively. In the present system shown schematically in Fig. S9, the pseudospin degree of freedom can be conveniently interpreted as Sn_{top} and Sn_{bottom} atoms distinguished by their vertical distances away from the substrate. In Eq. (1), $h_0(\vec{k})$ describes a gapless Dirac cone. Hamiltonian $h_{sub}(\vec{k})$ captures the difference of the chemical potentials between the Sn_{to} and Sn_{bottom} atoms, $\delta\mu = \mu_{top} - \mu_{bottom}$, which opens a band gap at the Dirac point. The SOC effect is described by $h_{soc}(\vec{k})$ with Δ denoting the magnitude of the SOC gap. Since the inversion symmetry is naturally broken in the presence of the substrate, $h_R(\vec{k})$ is introduced to account for Rashba-type SOC, where λ denotes the

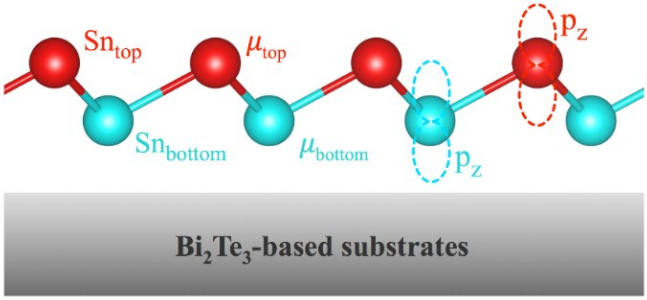

corresponding coupling strength.

Fig. S9 Schematic illustration of stanene grown on Bi_2Te_3-based substrates. Sn_{top} and Sn_{bottom} label two types of Sn atoms distinguished by the vertical distances between the respective atoms and substrates.

As discussed in the main text, the lack of a global band gap in the present systems hinders a straightforward definition of their topological properties. Here, we only focus on investigating the possibility of the SOC-induced band inversion around the K or K' point. For convenience, we choose the K point as an example, where $\eta = 1$. A close inspection of the effective model reveals that h_{sub} leads to the polarization of the pseudospin around the K point while the SOC effect results in the depolarization of the pseudospin. Therefore, the pseudospin polarization around the conduction band minimum (CBM) or valence band maximum (VBM) is a good probe to detect the potential SOC-induced band inversion.
In the present study, the expectation value of the pseudospin polarization is defined as

$$\rho_{c,v} = \langle \psi_{c,v} | \sigma_z s_0 | \psi_{c,v} \rangle , \qquad (5)$$

where $\psi_{c,v}$ denote the eigenstates of the conduction band and valence band, respectively. The SOC-induced band inversion is characterized by the sign change of ρ_c or ρ_v at the CMB or VBM. In the absence of SOC, we find ρ_c is either positive or negative definitely depending on the sign of $\delta\mu$, indicating that Rashba-SOC cannot solely lead to the band inversion. In contrast, the presence of SOC results in the band gap closing at

$$\Delta_c = \frac{1}{2}\left(\delta\mu + \sqrt{\delta\mu^2 + \lambda^2}\right). \qquad (6)$$

By increasing the SOC from the range of $\Delta < \Delta_c$ to $\Delta > \Delta_c$, ρ_c and ρ_v exchange the signs.

By comparing the signs of ρ_c or ρ_v of the investigated system before and after turning on the SOC, we can directly identify whether the band inversion occurs. In Fig. S10, we depict a schematic to illustrate the developed pseudospin-based approach for identifying the SOC-induced band inversion. For the present systems, this approach is very useful because the pseudospin polarization ρ of a band is actually the difference between the Sn_{top} and Sn_{bottom} components of that band, the value of which can be easily obtained via the standard fist-principles calculations. It is worthwhile to point out that the validity of this pseudospin-based method is not merely limited in the present study.

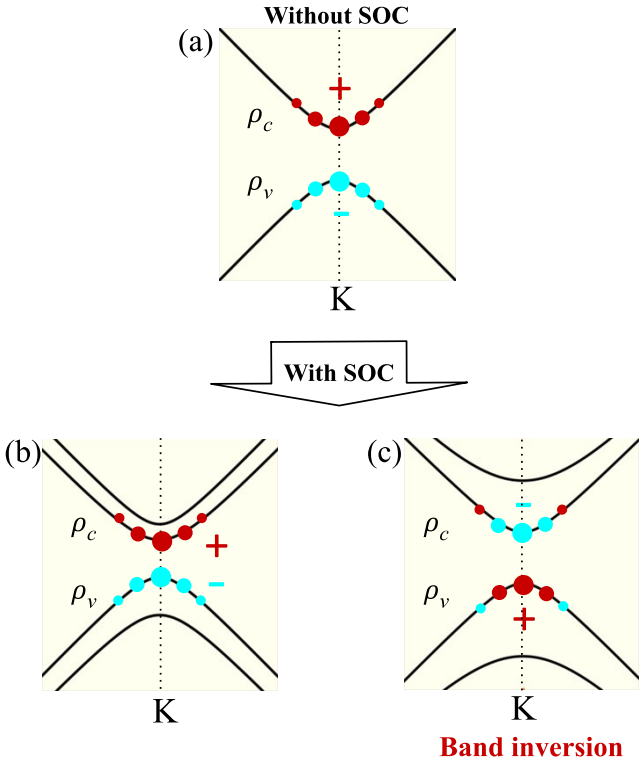

Fig. S10 Schematic illustration of the pseudospin-based approach for identifying the absence or existence of the SOC-induced band inversion. (a) Band structure without SOC, where ρ_c and ρ_v possess respectively positive and negative signs. (b) Band structure with SOC, where ρ_c and ρ_v do not change signs, indicating that the SOC does not invert the bands. (c) Band structure with SOC, where ρ_c and ρ_v exchange signs at the K point, indicating that the SOC is sufficiently strong to invert the bands.

References

1. R. W. G. Wyckoff, *Crystal structures*, John Wiley & Sons, New York, 2nd edn., 1964.
2. A. H. Castro Neto, F. Guinea, N. M. R. Peres, K. S. Novoselov and A. K. Geim, *Rev. Mod. Phys.*, 2009, **81**, 109-162.
3. C.-C. Liu, H. Jiang and Y. Yao, *Phys. Rev. B*, 2011, **84**, 195430.